J. Fluid Mech. (2010), *vol.* 663, *pp.* 160–179. © Cambridge University Press 2010
doi:10.1017/S0022112010003447

Turbulence measurements using a nanoscale thermal anemometry probe

SEAN C. C. BAILEY[1]†, GARY J. KUNKEL[1]‡, MARCUS HULTMARK[1], MARGIT VALLIKIVI[1], JEFFREY P. HILL[1]¶, KARL A. MEYER[1]‖, CANDICE TSAY[2], CRAIG B. ARNOLD[1] AND ALEXANDER J. SMITS[1]

[1]Department of Mechanical and Aerospace Engineering, Princeton University, Princeton, NJ 08544, USA

[2]Department of Electrical Engineering, Princeton University, Princeton, NJ 08544, USA

(Received 26 May 2010; revised 24 June 2010; accepted 24 June 2010; first published online 1 September 2010)

A nanoscale thermal anemometry probe (NSTAP) has been developed to measure velocity fluctuations at ultra-small scales. The sensing element is a free-standing platinum nanoscale wire, $100\,\text{nm} \times 2\,\mu\text{m} \times 60\,\mu\text{m}$, suspended between two current-carrying contacts and the sensor is an order of magnitude smaller than presently available commercial hot wires. The probe is constructed using standard semiconductor and MEMS manufacturing methods, which enables many probes to be manufactured simultaneously. Measurements were performed in grid-generated turbulence and compared to conventional hot-wire probes with a range of sensor lengths. The results demonstrate that the NSTAP behaves similarly to conventional hot-wire probes but with better spatial resolution and faster temporal response. The results are used to investigate spatial filtering effects, including the impact of spatial filtering on the probability density of velocity and velocity increment statistics.

Key words: MEMS/NEMS, turbulent flows

1. Introduction

Hot-wire anemometry has proven to be an essential tool in experimental fluid mechanics, particularly in the study of turbulence. However, a major drawback of hot-wire anemometry is the finite length of the wire, l_w, so that the measured velocity is spatially averaged by the sensor such that

$$\boldsymbol{u}(x_1^*, x_2^*, x_3^*) = \frac{1}{l_w} \int_{-l_w/2}^{l_w/2} \boldsymbol{u}_a(x_1^*, x_2, x_3^*)\, \mathrm{d}x_2, \tag{1.1}$$

where the origin of $\boldsymbol{x}^*$ is located at the centre of the wire, and the x_1, x_2 and x_3 directions are as shown in figure 1. The true velocity is denoted by $\boldsymbol{u}_a$ and the measured velocity by $\boldsymbol{u}$.

† Present address: Department of Mechanical Engineering, University of Kentucky, Lexington, KY 40515, USA. Email address for correspondence: scbailey@engr.uky.edu

‡ Present address: Seagate Technology, Bloomington, MN 55435, USA

¶ Present address: Aero/Fluids/Performance Group, Lockheed Martin Space Systems, Sunnyvale, CA 94086, USA

‖ Present address: MITRE Corporation, McLean, VA 22102, USA

https://doi.org/10.1017/S0022112010003447 Published online by Cambridge University Press

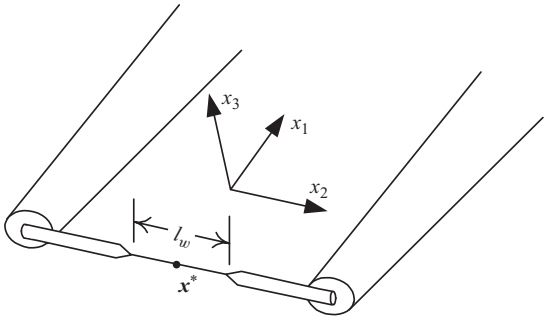


FIGURE 1. Schematic illustrating hot-wire coordinate system.

One of the earliest investigations of spatial filtering was performed by Wyngaard (1968), who transformed (1.1) to Fourier space to find

$$\boldsymbol{u}(x_1^*, x_2^*, x_3^*) = \int_{-\infty}^{\infty}\int_{-\infty}^{\infty}\int_{-\infty}^{\infty} \frac{\sin(k_2 l_w/2)}{k_2 l_w/2}\hat{\boldsymbol{u}}_a(k_1, k_2, k_3) \times \exp[\mathrm{i}(k_1 x_1 + k_2 x_2 + k_3 x_3)]\,\mathrm{d}k_1\,\mathrm{d}k_2\,\mathrm{d}k_3, \quad (1.2)$$

where $\boldsymbol{k} = (k_1, k_2, k_3)$ is the wavenumber vector. We see that spatial averaging causes the sensor to act as a filter, and the contribution to the velocity fluctuations from eddies smaller than the wire length is lost. The one-dimensional energy spectrum measured by a finite sensor, E_{11}, is therefore related to the full three-dimensional energy spectrum, $E_a(|k|)$, through

$$E_{11}(k_1) = \int_0^{\infty}\int_0^{\infty}\left[\frac{\sin(k_2 l_w/2)}{k_2 l_w}\right]^2 \frac{E_a(|k|)}{4\pi|k|^4}\left(|k|^2 - k_1^2\right)\mathrm{d}k_2\,\mathrm{d}k_3. \quad (1.3)$$

Equation (1.3) illustrates how spatial averaging in the k_2 direction can be aliased to all scales in the k_1 direction, as demonstrated experimentally by Citriniti & George (1997). Wyngaard (1968) used this analysis to examine the effects of spatial filtering on hot-wire measurements in homogeneous isotropic turbulence by modelling $E_a(|k|)$ using the Pao spectrum to describe the high-wavenumber contributions to the signal. This work has since been extended for homogeneous isotropic turbulence by several authors, including Ewing, Hussein & George (1995), who used the full Kármán–Saffman–Pao model spectrum.

These analytical models give important insights into the effects of spatial filtering, but they are not useful for developing correction schemes for measurements of anisotropic turbulence where the spectra are not known *a priori*, such as in turbulent wall-bounded flows. This problem is particularly evident at high Reynolds numbers, where, in many laboratory experiments, the smallest scales of turbulence are much smaller than the wire length. Ligrani & Bradshaw (1987*a*) suggested that hot-wire probes will only produce reliable statistics when $l_w^+ \leqslant 20$, where $l_w^+ = l_w u_\tau/\nu$. Here, $u_\tau = \sqrt{\tau_w/\rho}$, τ_w is the stress at the wall, and ρ and ν are the fluid density and kinematic viscosity, respectively. More recently, Hutchins *et al.* (2009) provided an empirical correlation to help estimate the filtering effects (at $y^+ = 15$) as a function of three parameters: $\delta^+ = \delta u_\tau/\nu$, l_w^+ and l_w/δ, where δ is the boundary-layer thickness, and Chin *et al.* (2009) proposed a correction to the measured one-dimensional spectrum based on the spatial filtering effect of a finite-length wire on the three-dimensional spectra in a channel flow obtained by direct numerical simulation.

https://doi.org/10.1017/S0022112010003447 Published online by Cambridge University Press

In the literature on wall-bounded flows, it is generally assumed that the relevant parameter for spatial filtering is l_w^+. It can also be argued that the relevant length scale for spatial filtering effects should be the Kolmogorov length scale η, rather than the viscous length scale ν/u_τ. The two scales are proportional close to walls (Yakhot *et al.* 2010), but the difference may be important further away. Whether l_w/η or l_w^+ is the most general parameter to describe the spatial resolution of a probe is still an open question. It is, however, clear that accurate studies of the characteristics of such small-scale motions requires very small probes.

One experiment where the effects of spatial filtering are particularly evident is the Princeton/ONR Superpipe experiment described by Zagarola & Smits (1998) and Morrison *et al.* (2004). By operating at pressures up to 200 atm, pipe-flow Reynolds numbers up to 38×10^6 can be achieved. With a fixed outer scale of the flow, an increase in Reynolds numbers necessarily means a decrease in the physical size of the smallest scales of turbulence. For example, in pipe flows, the ratio of the size of the largest scale motions to the smallest scale motions can be represented by $R^+ = Ru_\tau/\nu$, which, at the highest Reynolds numbers obtained in the Superpipe, has a value of 5.3×10^5. Here, R is the radius of the pipe. For a conventional hot-wire probe at these conditions, $l_w^+ \approx 4000$. Therefore, in order to perform fully resolved turbulence measurements in facilities such as the Superpipe, it is necessary to significantly reduce the size of the sensor.

It is not possible to reduce the probe size by simply reducing its length since there is an important additional restriction imposed by end-conduction effects. For these effects to be small enough to be neglected, l_w/d needs to be large enough, where d is the wire diameter. Perry, Smits & Chong (1979), Ligrani & Bradshaw (1987*a*) and Klewicki & Falco (1990) recommended that $l_w/d \geqslant 200$, although Li *et al.* (2004) pointed out that the ratio can be reduced to about 100 at a high Biot number, such as that experienced in the Superpipe at high Reynolds numbers. Because of this limitation on the wire length, a wire with a sufficiently small length to capture the smallest turbulence scales at a high Reynolds number will require a diameter that is smaller than what is presently available.

A number of efforts have tried to address these issues by using conventional hot-wire construction techniques to make shorter wires. Willmarth & Sharma (1984), for example, used Wollaston wire of $d = 0.5\,\mu\text{m}$ and created probes as small as $l_w = 50\,\mu\text{m}$. Unfortunately, these data suffered from end-conduction effects. Ligrani & Bradshaw (1987*a*,*b*) used a similar probe design with $d = 0.625\,\mu\text{m}$, but with the requirement that $l/d \geqslant 200$, the smallest possible wire length was $125\,\mu\text{m}$. Löfdahl, Stemme & Johannson (1989) and Löfdahl, Stemme & Johannson (1992) instead developed single- and dual-component velocity sensors using MEMS manufacturing techniques. These probes gave results that compared well to conventional hot-wire probes, but the largest dimension of the probe-sensing area was $400\,\mu\text{m}$, offering only a slight improvement in spatial resolution over conventional probes. Jiang *et al.* (1994), Ho *et al.* (1993) and Tai *et al.* (1993) also used MEMS techniques to manufacture a thermal anemometry probe with a geometry similar to conventional hot wires, although the sensing element was made of polysilicon. These probes were a great improvement in terms of spatial dimensions, with the smallest having a length of $10\,\mu\text{m}$, but they had low aspect ratios, and end-conduction effects introduced multiple time scales into the frequency response. Low aspect ratios were also present in the multi-component hot-wire probe produced by Chen *et al.* (2003), with sensor dimensions as small as $50\,\mu\text{m} \times 6\,\mu\text{m} \times 2.7\,\mu\text{m}$. In this instance, the sensing element was in close proximity to a substrate, making them impractical for conventional turbulence measurements.

https://doi.org/10.1017/S0022112010003447 Published online by Cambridge University Press

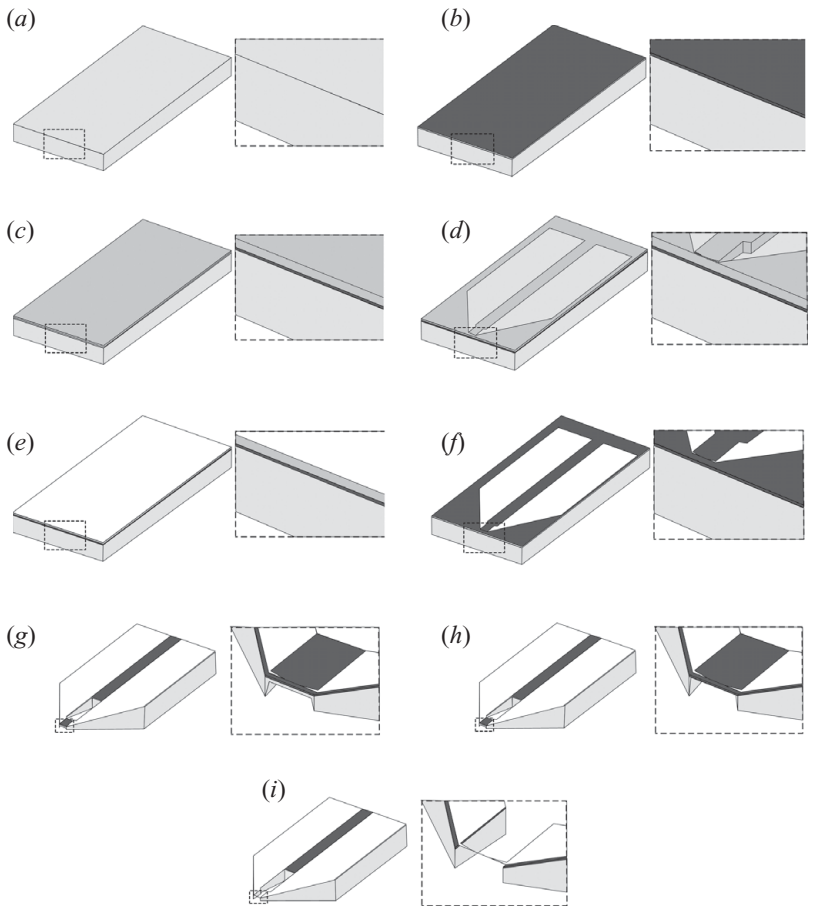


FIGURE 2. Schematic of the fabrication procedure: (*a*) bare wafer, (*b*) oxide-layer growth, (*c*) spin-coat on photoresist, (*d*) photolithography, (*e*) metal deposition, (*f*) metal lift-off, (*g*) precision laser micromachining, (*h*) reactive ion etching and (*i*) completed probe after buffered oxide etch.

Here, we have two purposes. First, we describe the design and testing of a nanoscale thermal anemometry probe (NSTAP) that can measure instantaneous fluctuating velocities at ultra-small scales, without the limitations and problems encountered in previous attempts to build small sensors. With a platinum sensing element two orders of magnitude smaller than current commercial technology, the spatial and temporal resolution of the NSTAP greatly exceeds existing systems. Second, we use the NSTAP together with an array of conventional hot-wire probes to quantify the effects of spatial resolution on the measurement of grid turbulence, and to demonstrate the superior spatial and temporal resolutions of the NSTAP.

2. NSTAP construction

Manufacturing the NSTAP uses a series of standard semiconductor and MEMS manufacturing techniques to produce a free-standing nanoscale wire between two electrically conducting supports. The initial probe design and manufacture was described by Kunkel, Arnold & Smits (2006), and the present steps are illustrated in figure 2(*a–i*).

https://doi.org/10.1017/S0022112010003447 Published online by Cambridge University Press

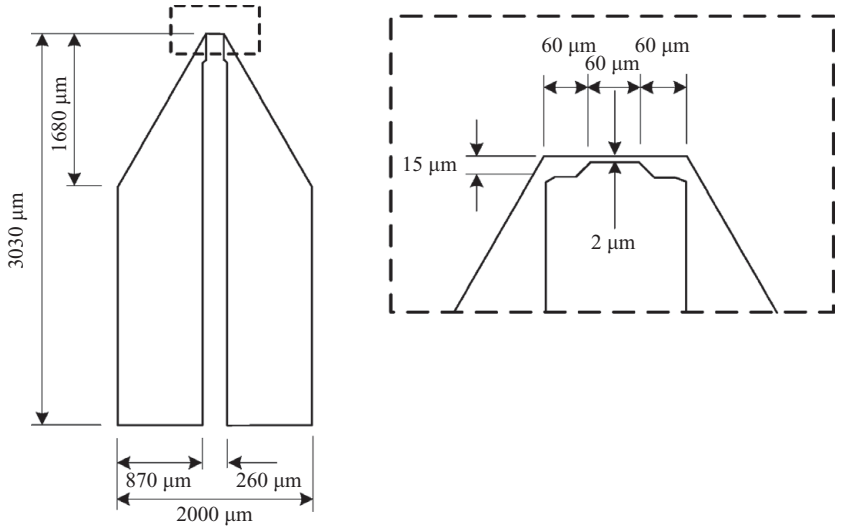


FIGURE 3. Sketch of the probe geometry showing dimensions of contact pads and wire.

The procedure starts with a standard 381 mm silicon wafer approximately 525 μm thick (figure 2*a*). An ∼500 nm thick layer of SiO_2 is grown on the silicon wafer using plasma-enhanced chemical vapour deposition (PECVD) (figure 2*b*). This oxide layer acts as an insulating layer between the metal and the silicon substrate. In addition, the oxide layer performs the important duty of supporting the metal nanoscale wire during the manufacturing process.

Photoresist is spin-coated on the surface of the wafer (figure 2*c*) and standard optical lithographic techniques are used to pattern the probe shape into the photoresist (figure 2*d*). Several hundred probes can be patterned onto a single wafer. A single probe pattern is shown in figure 3, and this pattern forms the basic geometry of the NSTAP. Each probe consists of two 3.03 mm × 0.87 mm contact pads narrowing at the front of the probe (to reduce the aerodynamic interference) connected to a nominally 2 μm × 60 μm wire through two 15 μm × 60 μm long stubs. The stubs between the wire and the probe pads thermally separate the hot wire from the relatively large-probe-contact pads (Li *et al.* 2004). Note that the probe design called for a 1 μm × 60 μm wire; however, limitations of the photolithography process results in the manufactured dimension of 2 μm × 60 μm.

An electron beam evaporator is then used to deposit a 10 nm layer of titanium on the front side of the wafer (to promote adhesion) followed by a 100 nm thick layer of platinum (figure 2*e*). This thickness of the platinum becomes the nanoscale wire dimension perpendicular to the flow. After deposition, unwanted platinum is lifted off using a solution of PRS-1000 at 100 °C, leaving the platinum on the surface of the wafer in the pattern defined during the photolithography procedure (figure 2*f*).

A pulsed UV laser (wavelength of 355 nm, pulsewidth of 30 ns) combined with a high-precision motion control system is used to machine the back side of the silicon wafer, shaping the supports so as to minimize their aerodynamic interference and cut the probe from the wafer (figure 2*g*). The ablative nature of the process imposes limitations on the accuracy of the micromachining; so a thin layer of silicon is intentionally left between the support structure immediately below the nanoscale wire to prevent accidental destruction of the wire during micromachining. This layer is removed using

https://doi.org/10.1017/S0022112010003447 Published online by Cambridge University Press

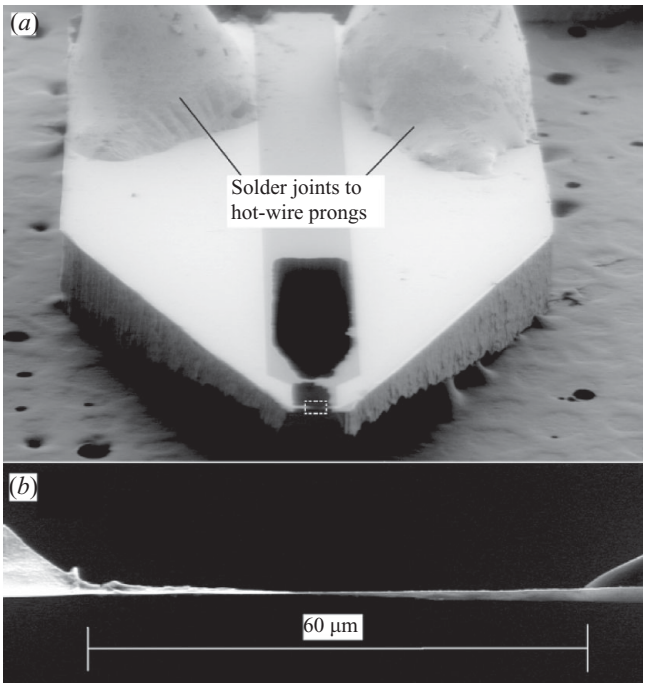


FIGURE 4. A scanning-electron-microscope image of the completed NSTAP showing (*a*) the whole probe and (*b*) a close-up of the region indicated by a dashed box showing wire sensing length.

a dry reactive-ion etch of SF_6 and O_2 (figure 2*h*). During this process, the platinum layer of the probe is protected by adhering the platinum-coated surface to a glass slide with wax, leaving only the silicon exposed to the chemically reactive plasma. Etching is performed at relatively slow rates with regular inspection to ensure that the layer of SiO_2 supporting the nanoscale wire is maintained. This SiO_2 layer prevents damage to the nanoscale wire by acting as a buffer between the wire and the plasma.

Following immersion in an acetone bath to remove any residual wax, the probe is mounted onto conventional hot-wire prongs using soldering. This step is typically performed before removal of the SiO_2 as it helps to support the nanoscale wire during handling. The final manufacturing step is removal of the SiO_2 between the contact pads using buffered oxide etch solution (figure 2*i*). A scanning-electron-microscope image of a typical probe is shown in figure 4. Note that the probe shown in figure 4 has a small (approximately 20 μm × 20 μm) bridge of silicon downstream of the sensor. This bridge is an artefact of imperfections introduced during the laser-micromachining and reactive-ion-etching processes and is not present in all probes. Data taken using probes with such bridges and without indicated that these bridges did not introduce adverse effects at the location of the sensor.

Upon completion, a free-standing wire with dimensions of 100 nm × 2 μm × 60 μm and electrical resistance of approximately 200 Ω is left between the two support structures.

3. NSTAP operating characteristics

The operating principle of the NSTAP is identical to that used in conventional thermal anemometry (Bruun 1995), whereby an electric current is passed through

https://doi.org/10.1017/S0022112010003447 Published online by Cambridge University Press

the sensor heating it above the ambient fluid temperature. As the fluid flows over the wire, the convective heat transfer to the fluid cools the wire. In constant-current (CCA) operation, the current is maintained at a constant value and the change in wire resistance due to a change in velocity manifests itself as a change in the voltage across the wire. In constant-temperature (CTA) operation, the current to the wire is instead adjusted to maintain a constant wire resistance through a feedback circuit, and the voltage output is again a function of the flow velocity. Once the anemometer is calibrated, it can be used to measure the mean and fluctuating velocity of the fluid flow. NSTAPs have been successfully operated in both a purpose-built uncompensated CCA circuit used during initial testing as well as a Dantec Streamline CTA system in 1 : 1 mode, balanced using an external resistor.

It was found that annealing of the probe was essential. Staring with an initial resistance of about 200 Ω, the resistance stabilized after the probe was operated for at least 24 h at high temperature, resulting in a typical final cold resistance of about 140 Ω.

The thermal coefficient of resistance, χ, of the NSTAP was measured using a heated wind tunnel and found to be 0.0019 K^{-1}. A typical value for a 90 % platinum, 10 % rhodium hot wire is 0.0018 K^{-1}.

3.1. *Temporal response*

We expect that, compared to a conventional hot-wire probe, the temporal response of the NSTAP will be greatly improved due to its reduced thermal mass. The response of the probe to a square-wave voltage input in an uncompensated CCA circuit was measured at flow velocities ranging from 8 to 40 m s^{-1}. Under these conditions, the time constant was found to be between 3.4 and 3.6 μs (corresponding to a 3 dB frequency response of approximately 9 kHz), which is almost three orders of magnitude shorter than the corresponding time constants of $O(1\,\mathrm{ms})$ for conventional hot-wire probes in CCA (Tavoularis 2005). However, as discussed by Li (2006) and others, the step response of a probe to a voltage perturbation overestimates the frequency response of the probe to velocity perturbations. The NSTAP response to a step change in velocity was therefore estimated using the local heat balance along a hot-wire probe (as described in Comte-Bellot & Foss 2007, for example). For a wire with arbitrary cross-section, under the assumption that the local wire temperature, T, is only a function of x_2 and time, t, the local heat balance appears as

$$\tau \frac{\partial T}{\partial t} = \frac{\partial^2 T}{\partial x_2^2} + C\,(T - T_a) + D, \tag{3.1}$$

with

$$\tau = \frac{\rho_w c_w}{k_w}, \tag{3.2}$$

$$C = \frac{\chi R_0 I^2}{k_w A^2} - \frac{Nu}{\ell}\frac{k_a}{k_w}\frac{P}{A}, \tag{3.3}$$

and

$$D = \frac{R_0 I^2}{k_w A^2}, \tag{3.4}$$

where ρ_w, c_w, R_0, χ and k_w are the density, specific heat, resistivity, thermal coefficient of resistance and thermal conductivity of the wire material, respectively, at temperature T. The wire geometry is described using the area A and perimeter P of the wire cross-section, and the length scale ℓ used in the definition of the Nusselt

https://doi.org/10.1017/S0022112010003447 Published online by Cambridge University Press

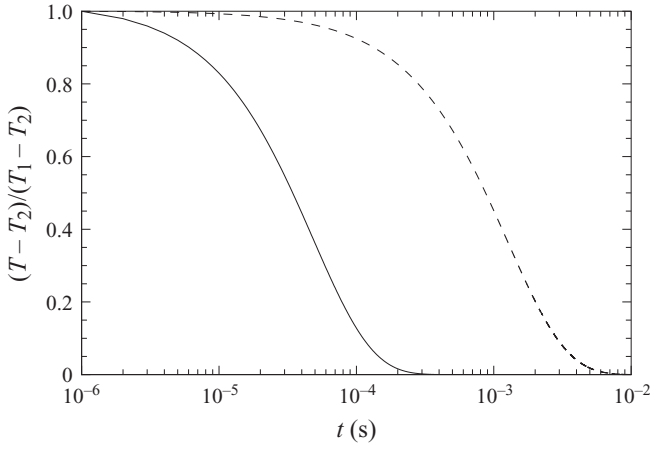


FIGURE 5. Comparison of temporal response of the NSTAP for a step change in Nu to that of a 5 µm tungsten hot wire, based on the solution of (3.1). Solid line, NSTAP; dashed line, hot wire.

number, Nu, where for a round wire $\ell = d$, while for the NSTAP we use the long dimension of the wire cross-section. The flow conditions are contained in Nu, k_a, the thermal conductivity of air at the film temperature, and T_a, the temperature of the air flow. The temperature increase of the wire is driven by Joule heating through the current I. Equation (3.1) was solved numerically for a step increase in the Nusselt number under the assumption of zero temperature variation along the length of the wire and a constant wire current. The results shown in figure 5 indicate that a probe with the NSTAP geometry has an expected time constant for velocity perturbations of about 50 µs, which is considerably slower than its response to a voltage perturbation, but it is still at least an order of magnitude faster than that of a conventional 5 µm diameter tungsten hot wire, where this analysis gave 1.3 ms, which is in good agreement with the experimental value reported by Tavoularis (2005).

3.2. *End-conduction effects*

End conduction also attenuates the dynamic response of the probe (as recently discussed by, for example, Morris & Foss 2003 and Li 2004) by attenuating heat waves along the wire. For a typical hot wire, these take effect at a frequency proportional to $k_w/(\rho_w c_w l_w^2)$ (Li 2004). For a conventional probe, such as a 5 µm, 1 mm tungsten hot wire, this attenuation is expected to occur for $f > O(100\,\mathrm{Hz})$, whereas for the NSTAP probe, the attenuation will occur for $f > O(10\,\mathrm{kHz})$ due to the significantly smaller wire length. Therefore, the additional time constant imposed by end-conduction effects will have a greatly reduced impact on the NSTAP measurements compared to those made using conventional probes.

We also need to address the criteria for minimizing end-conduction losses. For conventional probes, it is generally assumed that end-conduction effects are negligible when $l/d > 200$. Due to its non-cylindrical geometry, this criterion cannot be applied directly to the NSTAP, although some conclusions can be made using the steady-state solution to (3.1). That is (Comte-Bellot & Foss 2007),

$$T - T_a = \frac{D}{C}\left(1 - \frac{\cosh\left(C^{1/2}x_2\right)}{\cosh\left(C^{1/2}l_w/2\right)}\right). \tag{3.5}$$

https://doi.org/10.1017/S0022112010003447 Published online by Cambridge University Press

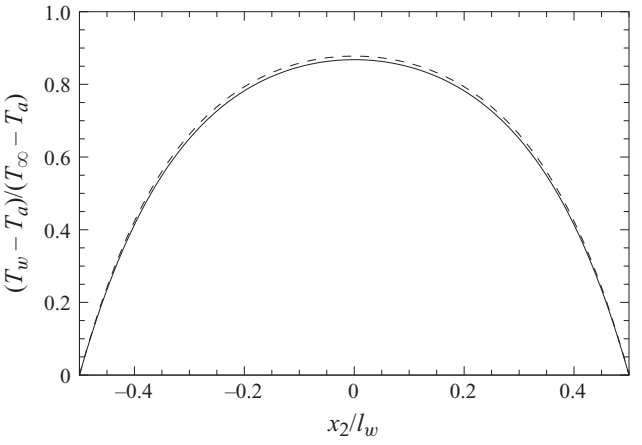


FIGURE 6. Calculated temperature distribution of the NSTAP compared to that of a 5 μm diameter, 1 mm long tungsten hot wire normalized using the temperature of an infinitely long wire, T_∞. Solid line, NSTAP; dashed line, hot wire.

Using this solution, we can compare the expected temperature distribution for the NSTAP to that of a 5 μm, 1 mm long tungsten hot wire. To perform this calculation, we assumed that the NSTAP sensing element can be treated as a thin plate, for which the relationship of Nu to the Reynolds number based on ℓ is equivalent to that of a cylinder increased by a factor of approximately 1.3 (Avilov & Decker 1994). The comparison at a mean flow velocity of $30\,\mathrm{m\,s^{-1}}$ and overheat ratio of 0.8, shown in figure 6, supports the notion that the temperature distribution of the NSTAP is comparable to that of a conventional hot wire with $l/d = 200$.

3.3. *Angular sensitivity*

To evaluate the importance of aerodynamic interference of the supporting silicon structure and the effect of the rectangular cross-section of the nanowire (2×0.1 μm), an experiment was conducted to evaluate the angular sensitivity of the probe. This was done by calibrating the probe at $\theta = 0°$, where $\theta = \tan^{-1}(U_3/U_1)$, and pitching the probe in a laminar flow in the range of $-60° < \theta < 60°$ at two different free-stream velocities, 10 and $20\,\mathrm{m\,s^{-1}}$. The ratio between the measured velocity magnitude and the true velocity magnitude is shown in figure 7 as a function of θ, and we see that the measured velocity magnitude can deviate by up to 15 % from the true velocity magnitude over this range of angles.

These results can be compared to aerodynamic interference effects for the prongs of conventional hot wires, which can be estimated using the analysis of Adrian *et al.* (1984), that is

$$U_{meas} = \left(U_1^2 + k^2 U_2^2 + h^2 U_3^2\right)^{1/2}, \tag{3.6}$$

where the coefficients k and h depend on the probe geometry. For a conventional probe, Adrian *et al.* (1984) found that $h \approx 1.02$ and the expected behaviour for a conventional probe, shown in figure 7, illustrates the much stronger sensitivity of the NSTAP to variations in the flow angle. This increased sensitivity is most likely due to the possibility of separation from the tilted 'ribbon-like' nanowire itself, in addition to the flow acceleration introduced by the support structure.

https://doi.org/10.1017/S0022112010003447 Published online by Cambridge University Press

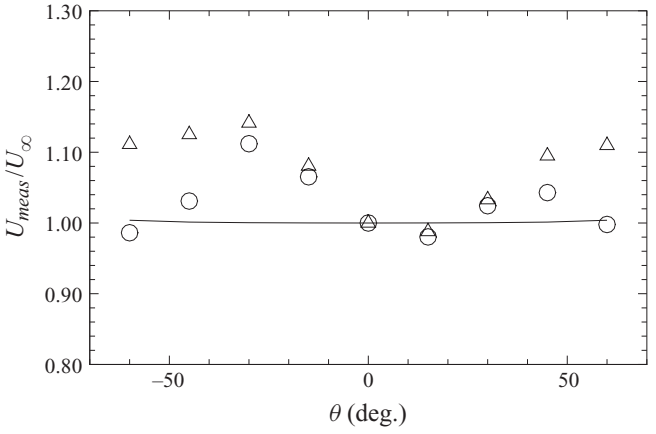


FIGURE 7. NSTAP sensitivity to the pitch angle at: △, 10 m s^{-1}; ○, 20 m s^{-1}, compared to a conventional hot wire estimated using (3.6) with $h = 1.02$ (solid line). Positive angles correspond to the metal side of the NSTAP facing the flow and negative to the silicon side facing the flow.

For the turbulence measurements reported here, θ was always less than 3° and the error introduced by angular sensitivity is expected to be less than 1 %. However, for accurate NSTAP measurements in flows with high turbulence intensity, further reductions in aerodynamic interference will be required, in combination with a reduction in the cross-sectional aspect ratio of the wire. Both modifications are being taken into consideration in an ongoing probe development, and it is acknowledged that the current NSTAP design is not suitable for flows where θ varies significantly.

3.4. *Heat-transfer regimes*

Finally, to ensure that the main mode of heat transfer is forced convection for all velocities of interest, three dimensionless parameters need to be considered: the Knudsen number Kn, the Richardson number Ri and the Péclet number Pe. The Knudsen number is the ratio of the mean free path of the fluid to the wire width ℓ. In air at atmospheric pressure, the mean free path is about 68 nm which, for the NSTAP, gives $Kn \approx 0.034$. Fingerson & Freymuth (1983) stated that the continuum assumption is adequate in this regime as long as density changes are small (Kn approximately constant), which is true for the flows of primary interest here. The Richardson number is the ratio of natural to forced convection. Because $Ri \propto \ell$, a smaller wire reduces the natural convection faster than the forced convection; thus, the critical Ri will occur at a lower velocity for the NSTAP compared to a conventional hot wire. The most critical parameter for the NSTAP was found to be the Péclet number, which is the ratio of convective to diffusive heat transfer ($Pe = Re \times Pr$, where Pr is the Prandtl number). Because $Re \propto \ell$, a smaller length scale will increase the relative importance of thermal diffusion in the fluid, resulting in a reduced sensitivity to velocity changes. This effect was observed in the NSTAP data for velocities lower than about 1.8 m s^{-1}. Figure 8 shows a calibration curve where the low-Péclet-number effect is seen for $Pe < 0.4$. This result corresponds well with the work by Avilov & Decker (1994), who investigated Péclet-number effects on cylinders and flat plates, and it is important to note that conventional heat-transfer correlations will not be valid for low Pe, and data taken under these conditions need to be treated with extra care.

https://doi.org/10.1017/S0022112010003447 Published online by Cambridge University Press

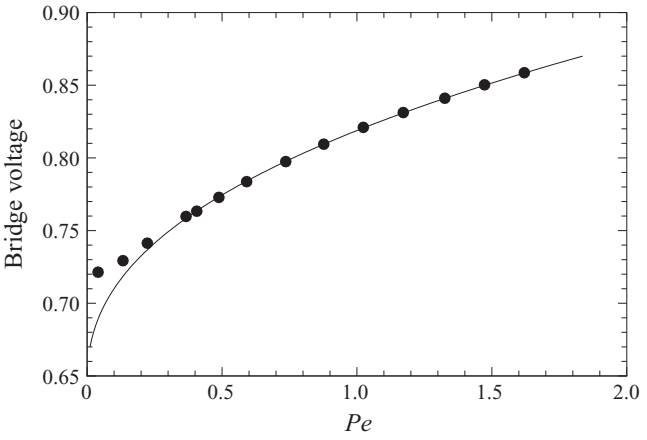


FIGURE 8. Low-Péclet-number effects can be seen for $Pe < 0.4$ on the calibration curve acquired with the NSTAP over large velocity range. Symbols are experimental data and solid line is a King's law fit.

4. Grid-turbulence measurements

To evaluate the performance of the NSTAP, and to assess spatial filtering effects, measurements were performed in grid-generated turbulence and compared to measurements using conventional hot-wire probes with different sensing lengths. The hot-wire probes were manufactured from platinum–10 % rhodium Wollaston wire with a diameter of 2.5 μm and sensing lengths of 0.5, 0.75, 1.0 and 1.5 mm, so that, in all cases, the wires exceeded the recommended length to diameter ratio of 200.

These tests were conducted using a Dantec Streamline CTA using the 1:1 bridge. The NSTAP was operated at $T_{hot} \approx 230\,^{\circ}\mathrm{C}$, resulting in a measured square-wave response of 150 kHz, whereas the hot wires were operated at a slightly higher temperature, $T_{hot} \approx 300\,^{\circ}\mathrm{C}$, resulting in a square-wave response between 50 and 70 kHz.

The probes were positioned near the centreline of a 0.6 m × 0.9 m × 3.6 m wind tunnel and mounted on a traverse capable of positioning the probes along the streamwise x_1-axis of the tunnel. The tunnel was equipped with a removable grid, which could be placed at the inlet of the test section to generate approximately homogeneous isotropic turbulence. The grid was made of cylindrical wires 3.2 mm in diameter welded to form a square mesh with mesh size $M = 25.4$ mm and a solidity of 0.23.

Measurements were performed at nominal free-stream velocities U_∞ of 10, 20 and 30 m s^{-1}, and at 10 streamwise positions ranging from $21M$ to $66M$ downstream of the grid, in intervals of $5M$. The dissipation rate, ϵ, was estimated using the turbulent kinetic energy decay rate assuming locally homogeneous isotropic turbulence. In this calculation, the turbulent kinetic energy for each velocity was estimated by fitting a single power-law curve to the decay of $3/2\langle u_1^2\rangle$ measured by all probes, where $u_1(t) = U_1(t) - \langle U_1\rangle$ and $\langle\,\rangle$ denotes a time average. The Taylor microscale Reynolds numbers, $Re_\lambda = \lambda_g \langle u_1^2\rangle^{1/2}/\nu$, where λ_g is the transverse Taylor microscale, varied from 42 to 113, and the Kolmogorov length scale, η, varied from 90 to 400 μm, so that $0.2 < l_w/\eta < 17$ for the probes used.

4.1. *Static calibration*

Calibrations were performed *in situ*, without the grid in place, using a Pitot-static probe mounted in close proximity to the probes to measure the mean free-stream

https://doi.org/10.1017/S0022112010003447 Published online by Cambridge University Press

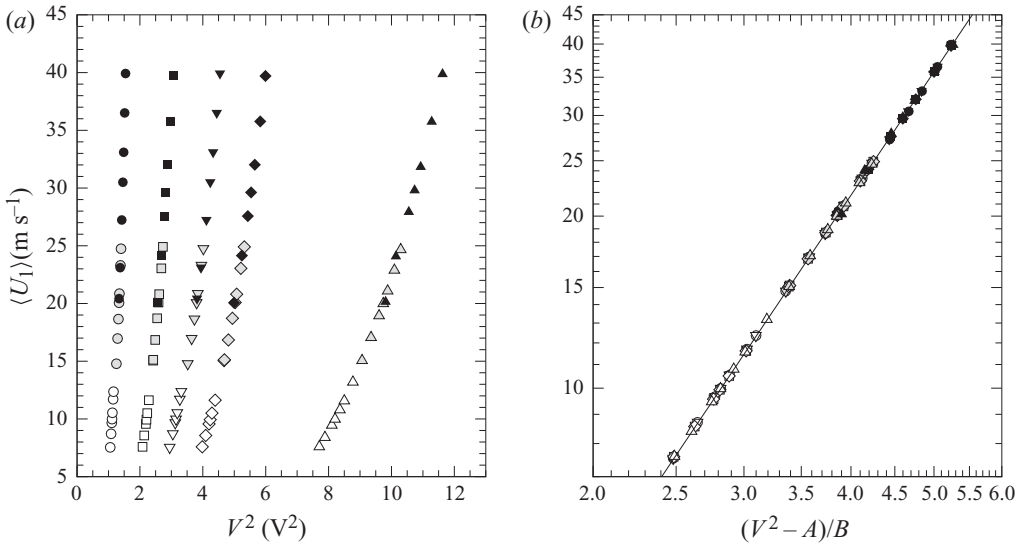


FIGURE 9. (*a*) Static calibration results for ○, NSTAP, and hot-wire probes of length □, 0.5 mm; ▽, 0.75 mm; ◇, 1.0 mm; and △, 1.5 mm. (*b*) Results scaled using the constants determined from least-squares fit to (4.1). Solid line is a power law with exponent of 0.45. Hollow, grey and solid symbols represent each of the three separate calibration runs.

velocity, $\langle U_1 \rangle$. Calibrations were performed before and after each grid turbulence measurement, and it was found that, once the initial annealing process was complete, there was no evidence of voltage drift. The measured bridge voltage, V, for each velocity is shown in the calibration curves in figure 9(*a*). (Note that each curve actually consists of three separate calibration runs taken at different times.) It can be seen in figure 9(*a*) that the reduction of sensitivity of the NSTAP is consistent with that observed with decreasing sensor diameter in conventional probes.

The static response of all probes was found to be well represented by King's law with an exponent of 0.45,

$$V^2 = A + B\langle U_1 \rangle^{0.45}, \tag{4.1}$$

where A and B are dimensional constants. This is shown in figure 9(*b*), which compares the scaled voltage, $(V^2 - B)/A$, to the calibration velocity. The agreement of the NSTAP response with King's law supports the assumption that the Reynolds-number dependence of the Nusselt number for the NSTAP geometry is similar to that of a cylinder, and confirms that the NSTAP static response is virtually identical to that of a conventional probe.

4.2. *Grid-turbulence decay*

The streamwise decay of the second and third moments of the streamwise velocity, $\langle u_1^2 \rangle$ and $\langle u_1^3 \rangle$, is shown in figure 10. We see that the decay of $\langle u_1^2 \rangle$ appears to follow the trend expected for grid-generated turbulence, but the behaviour of the third-order moment indicates that the turbulence was slightly inhomogeneous for $x_1/M < 40$. Further evidence of inhomogeneity was found during tests using two 0.5 mm diameter probes separated in the x_3 direction by a distance of $1.5M$, which revealed evidence of persistent wake effects from the grid elements for $x_1/M < 40$. Measurements from locations $x_1/M < 40$ were therefore not included in further data analysis.

https://doi.org/10.1017/S0022112010003447 Published online by Cambridge University Press

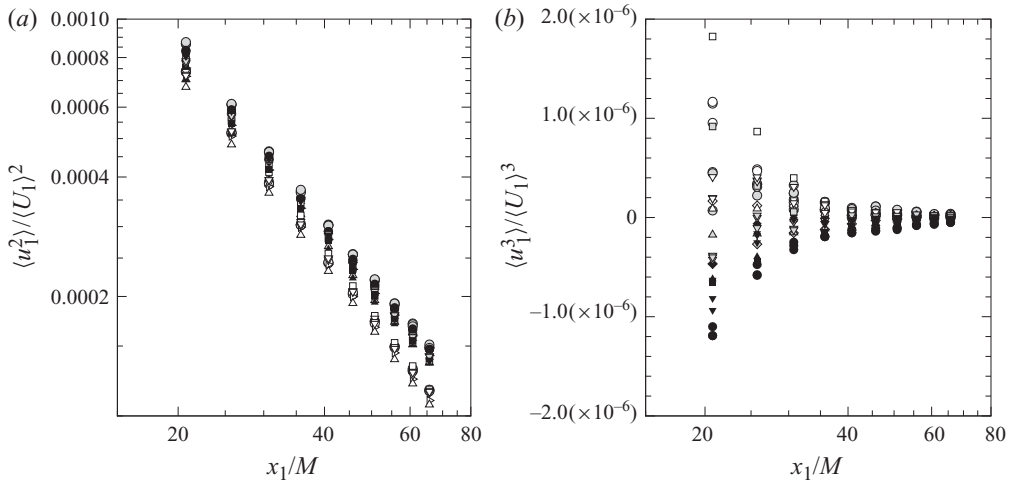


FIGURE 10. Measured (*a*) second and (*b*) third moments of velocity measured by ○, NSTAP; □, 0.5 mm probe; ▽, 0.75 mm probe; ◇, 1.0 mm probe; and △, 1.5 mm probe. Hollow symbols indicate $U_\infty = 10\,\mathrm{m\,s^{-1}}$, grey symbols indicate $U_\infty = 20\,\mathrm{m\,s^{-1}}$ and solid symbols represent $U_\infty = 30\,\mathrm{m\,s^{-1}}$.

4.3. *Spatial filtering effects on velocity statistics*

To illustrate the spatial filtering effects due to the limited probe size, the wavenumber spectra $E_{11}(k_1)$ are shown in figure 11, where the streamwise wavenumber is taken as $k_1 = 2\pi f/\langle U_1\rangle$ and f is the frequency. Figure 11(*a*) illustrates that the NSTAP provides virtually the same overall response as the conventional probes, even at low wavenumbers where end-conduction effects would manifest themselves. When viewed in pre-multiplied form, as in figure 11(*b*), the reduced spectral response of the larger probes becomes more obvious. At low Re_λ, the NSTAP and 0.5 mm probe are in excellent agreement and both measure an energy level that is slightly higher than that of the 1.5 mm probe. As Re_λ increases, the Kolmogorov length scale decreases so that l_w/η increases, and we see that the energy measured by even the 0.5 mm probe decreases relative to the NSTAP. It is also clear from figure 11(*b*) that the longer probes filter energy at wavelengths that are more than an order of magnitude larger than the wire length. As observed by, for example Citriniti & George (1997), this is not an unexpected result, and it is due to the action of the finite length of the wire as a spectral cut-off filter for small wavelengths in the direction parallel to the wire, leaving the normal directions relatively unfiltered. Because the filtering occurs in three-dimensional wavenumber space, when collapsed into the one-dimensional spectrum, the lost spectral energy is aliased among all streamwise wavelengths.

A more quantifiable measure of spatial filtering is provided by examining $\langle u_1^2\rangle/\langle u_N^2\rangle$, the ratio of the measured turbulence intensity to the value measured by the NSTAP under the same conditions (see figure 12). Although there is significant scatter in the data, $\langle u_1^2\rangle/\langle u_N^2\rangle$ decreases approximately linearly with increasing l_w/η from approximately 1 as $l_w/\eta \to 0$ to approximately 0.9 when $l_w/\eta \approx 10$.

Figure 12 also shows the energy loss found by integrating (1.3), which was solved numerically after modelling $E(|k|)$ using the Kármán–Saffman–Pao model spectrum. This model was applied for each combination of l_w/η and L/η, where L is the streamwise integral length scale measured in the experiments. Two observations can be made. First, due to the aliasing of filtering towards large scales, there is some l_w/L

https://doi.org/10.1017/S0022112010003447 Published online by Cambridge University Press

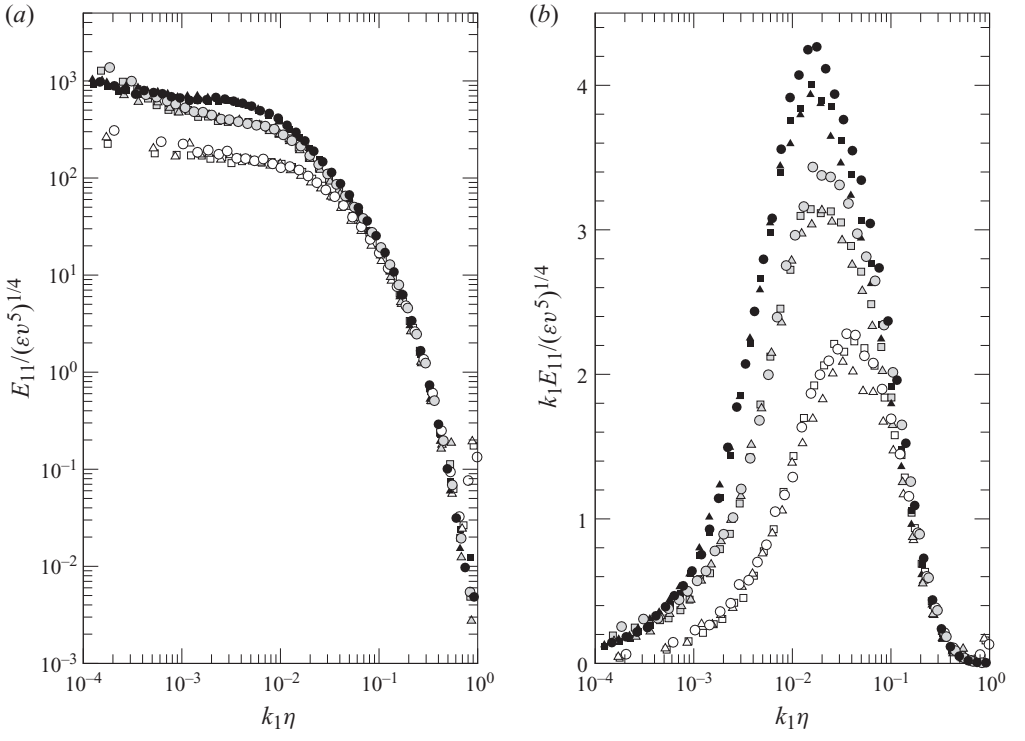


FIGURE 11. Measured streamwise wavenumber spectra normalized by the Kolmogorov scales in (*a*) standard and (*b*) pre-multiplied form. Results for ○, NSTAP; □, 0.5 mm probe; and △, 1.5 mm probe are shown for $Re_\lambda = 42$ (hollow symbols), $Re_\lambda = 66$ (grey symbols) and $Re_\lambda = 78$ (solid symbols).

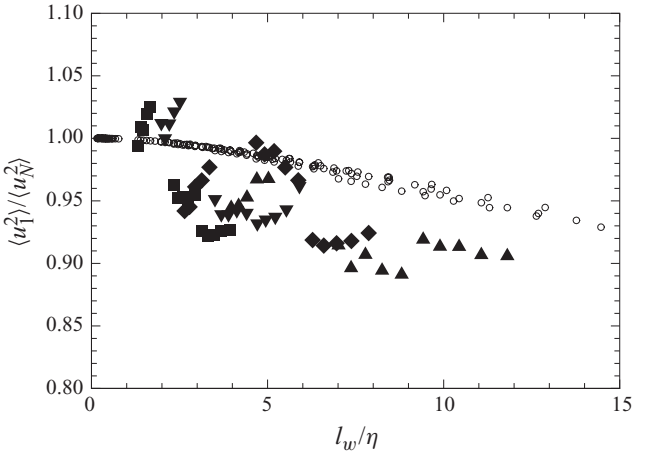


FIGURE 12. Streamwise Reynolds stress as a function of l_w/η. Value measured by: ■, 0.5 mm probe; ▼, 0.75 mm probe; ◆, 1.0 mm probe; and ▲, 1.5 mm probe, shown normalized by the value measured by the NSTAP. ○, values predicted using (1.3).

dependence introduced. Hence, although some of the scatter in figure 12 is likely due to experimental uncertainty, some of the scatter is also likely to be introduced by the L dependence of the filtered energy, which is not accounted for in this figure.

https://doi.org/10.1017/S0022112010003447 Published online by Cambridge University Press

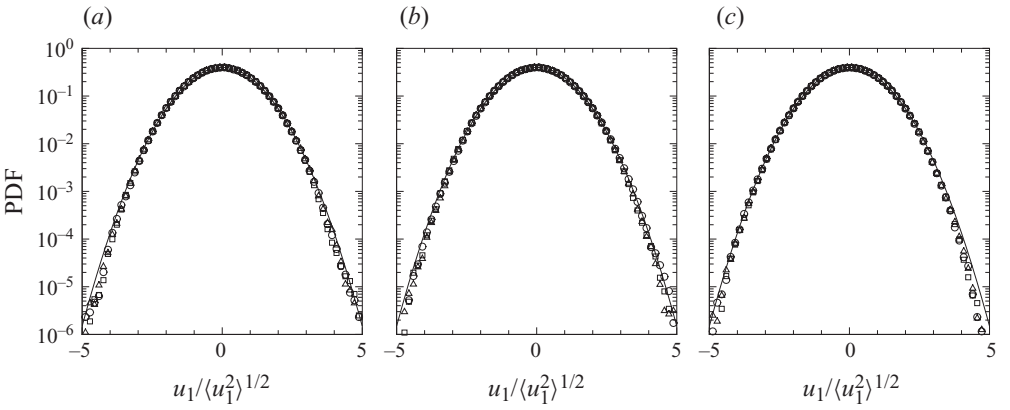


FIGURE 13. Measured p.d.f. of velocity for (*a*) $Re_\lambda = 42$, (*b*) $Re_\lambda = 66$ and (*c*) $Re_\lambda = 78$. Results for ○, NSTAP; □, 0.5 mm probe; and △, 1.5 mm probe are shown. Solid line is a Gaussian distribution.

Unfortunately, the range of η and L combinations in the current experiment were not sufficient to properly separate out the dependence of the filtering on each parameter. Second, the model underpredicts the filtering which occurred in the experiments. This may be due to the increased temporal response of the NSTAP relative to the conventional probes which would result in the normalization used in figure 12 to include the effects of both temporal and spatial filtering. In addition, Li (2004) and others have shown that the expected attenuation due to conduction effects can be up to 7 % for a conventional wire, and this filtered energy could also be contributing to the disagreement between the experimental results and the model, which does not take these effects into consideration.

In previous work on grid turbulence, considerable effort has been spent on investigating the spectral implications of spatial filtering on measurements of the velocity variance. The impact of spatial filtering on the higher order moments, and probability density function (p.d.f.) as a whole, has been largely overlooked. As illustrated in figure 13, the differences among the probes with different sensor lengths occur mainly in the tails of the p.d.f.s, so that spatial filtering becomes increasingly important when evaluating the higher order moments. This is illustrated quantitatively in figure 14, which shows the 4th-, 6th-, 8th- and 10th-order central moments measured by the conventional probes, normalized by the value measured by the NSTAP. Only the even moments are shown due to large scatter introduced into the normalization by the odd-ordered central moments by having a value near zero.

Figure 14 is illustrative in two respects. First, it provides further confidence in the NSTAP measurements due to the convergence towards unity as $l/\eta \to 0$. Second, it shows the systematic increase of the effects of spatial filtering with increased order of central moment. For example, when $l/\eta = 5$, the 10th-order moment has an error near 25 %, whereas the second-order moment has an error of approximately 5 % (a value which is within the range of typical measurement error).

The increased error with order of the velocity moment and the near-Gaussian properties of the underlying p.d.f. suggest that a correction can be applied to the measured moments to compensate for the spatial filtering. The simple correction,

$$\langle u_1^n \rangle_{corrected} = \langle u_1^n \rangle_{measured} G^{-0.27n}, \tag{4.2}$$

https://doi.org/10.1017/S0022112010003447 Published online by Cambridge University Press

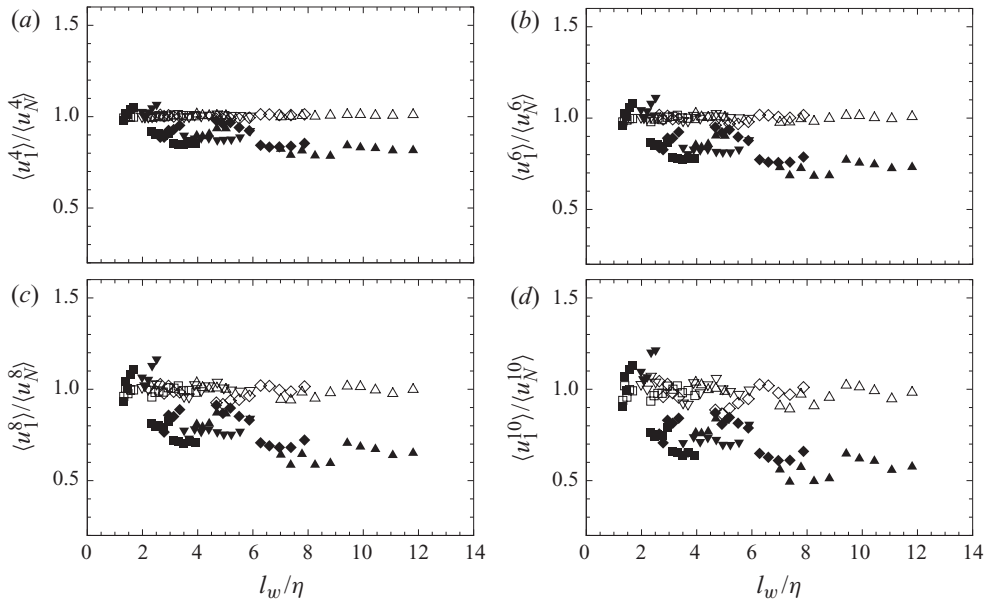


FIGURE 14. Higher order velocity moments as a function of l_w/η. Value measured by □, 0.5 mm probe; ▽, 0.75 mm probe; ◇, 1.0 mm probe; and △, 1.5 mm probe, shown normalized by the value measured by the NSTAP. Filled symbols are original data and hollow symbols are the values corrected using (4.2).

was found to be effective in minimizing the error, where n is the order of the central moment and G is the correction that would be applied to the second-order moment, for example as estimated by spectral modelling (that is, by using (1.3)). Here, G was approximated using $\langle u_1^2\rangle/\langle u_N^2\rangle$. As shown in figure 14, all the corrected values measured by the longer wires fall within 10 % of the values measured by the NSTAP, at least up to the 10th-order central moment.

4.4. *Spatial filtering effects on velocity-increment statistics*

Although the central moments, spectra and p.d.f.s of velocity provide much detailed information about the fluid velocity in turbulent flows, the structure of the turbulence is better revealed by the statistics of the velocity increment,

$$\delta\boldsymbol{u}(\boldsymbol{r}) = \boldsymbol{u}(\boldsymbol{x}+\boldsymbol{r}) - \boldsymbol{u}(\boldsymbol{x}), \tag{4.3}$$

where $\boldsymbol{r}$ is an arbitrary separation vector. In the current experiment, only the streamwise component of $\boldsymbol{u}$ was measured and the separation $\boldsymbol{r}$ was estimated using Taylor's hypothesis such that

$$\delta u_1(r_1) = u_1\left(t + \frac{r_1}{\langle U_1\rangle}\right) - u_1(t). \tag{4.4}$$

The p.d.f.s of δu_1 are shown in figure 15 for three separations. Once again, good general agreement is found among the probes, and the p.d.f.s clearly show the expected skewed appearance at small r_1, and tend towards being approximately Gaussian at large r_1.

A more detailed comparison among the probes can be conducted by normalizing the p.d.f.s of δu_1 measured by the 0.5 and 1.5 mm probes by the corresponding p.d.f.

https://doi.org/10.1017/S0022112010003447 Published online by Cambridge University Press

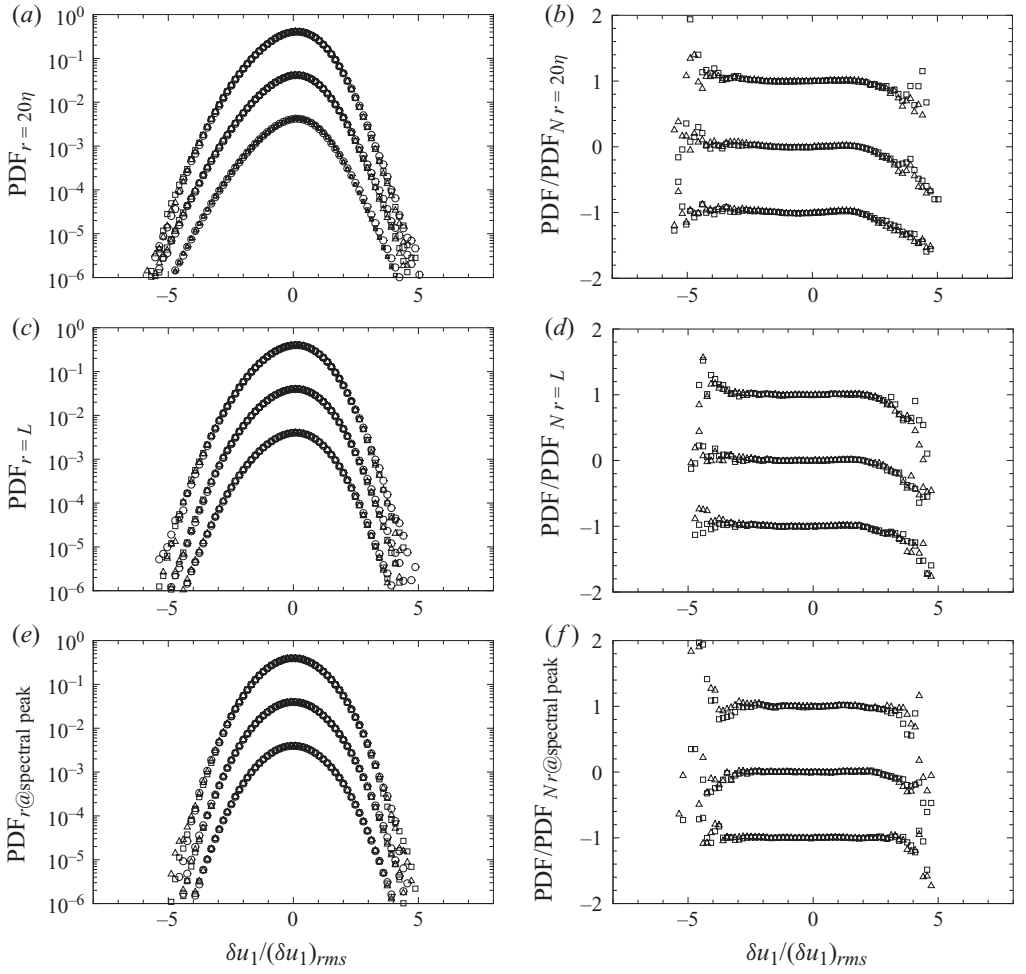


FIGURE 15. Measured p.d.f.s of δu_1 at (*a*) $r_1 = 20\eta$; (*c*) $r_1 = L$; (*e*) r_1 equal to the wavelength of maximum spectral content. Also shown are the same p.d.f.s normalized by the p.d.f. measured by the NSTAP at (*b*) $r_1 = 20\eta$, (*d*) $r_1 = L$ and (*f*) r_1 equal to the wavelength of maximum spectral content. ○, NSTAP; □, 0.5 mm probe; and △, 1.5 mm probe. Results are shown for $Re_\lambda = 42$, $Re_\lambda = 66$ and $Re_\lambda = 78$. Each successive Re_λ shifted down by a decade in (*a*), (*c*) and (*e*) and shifted down by 1 in (*b*), (*d*) and (*f*).

measured by the NSTAP, as shown in figure 15. As with the velocity p.d.f.s of figure 13, the differences among the three probes appear at the tails of the p.d.f.; however, the trend of decreasing agreement with increasing Reynolds number (that is, decreasing η) seen in the velocity statistics is no longer evident. Instead, the differences among the p.d.f.s is most evident at $\delta u_1/(\delta u_1)_{rms} > 2$, where the conventional hot-wire probes measure a lower probability of these events occurring. Either the conventional wires are measuring fewer deceleration events than the NSTAP, or the NSTAP is introducing more deceleration events. Both possibilities can be explained by the geometry of the NSTAP. In the case of the former, the smaller thermal mass of the NSTAP relative to the other probes (there is a 400 : 1 difference in volume between the NSTAP and 0.5 mm probe and 1200 : 1 between the NSTAP and 1.5 mm probe) will allow it to cool much faster when the flow velocity decreases, resulting in the probe capturing

https://doi.org/10.1017/S0022112010003447 Published online by Cambridge University Press

more of these events. In the case of the latter, the large support geometry surrounding the sensing wire could be decelerating small-scale structures through blockage.

5. Conclusions

We have shown that a new nanoscale hot-wire probe with dimensions $100\,\text{nm} \times 2\,\mu\text{m} \times 60\,\mu\text{m}$ has operating characteristics that are very similar to those of conventional hot-wire probes, but with considerably better spatial resolution and frequency response. We believe that this is the first time that a microscale hot wire free of end- or substrate-conduction effects has been constructed and successfully tested in a turbulent flow, opening the way for improved measurements of high-Reynolds-number flows. For example, a sensor of this scale will allow measurements at $l_w^+ = 20$ to be performed in the Superpipe facility for Reynolds numbers as high as 1.2×10^6 ($R^+ \approx 2.2 \times 10^4$). Further improvements are currently being sought by using electron beam lithography to reduce the sensing wire to dimensions of $100\,\text{nm} \times 100\,\text{nm} \times 20\,\mu\text{m}$, which will allow well-resolved measurements at Reynolds numbers up to 3.6×10^6 ($R^+ \approx 6.6 \times 10^4$) and also use deep reactive ion etching to improve the aerodynamic shaping of the probe.

Spatial filtering effects on turbulence were then evaluated by conducting measurements in grid turbulence with the new nanoscale probe and a number of conventional hot-wire probes. The biasing of spatial filtering effects to wavenumbers much larger than the sensor length was observed, in accordance with predictions from a commonly adopted model of spatial averaging effects. However, this model underestimates the magnitude of these effects, which may be due to the increased temporal response of the NSTAP. In addition, the impact of spatial filtering on higher order velocity moments was investigated and it was shown that a simple correction can be applied to recover these moments from underresolved sensors. Finally, the p.d.f.s of velocity increment statistics were investigated, and it was found that, at small spatial separations, the nanoscale probe measured high positive velocity increments with a slightly higher probability. Whether this result was due to the increased measurement accuracy of the nanoscale probe because of its better temporal and spatial resolutions, or if it was an artefact of increased blockage effects of the probe's support structure, is not yet clear. This difference will be investigated further using our new probe design, incorporating further streamlining of the sensor support structure.

While the immediate use for the new nanoscale probe is the study of small-scale turbulence, the construction of a free-standing nanoscale wire with aerodynamic supports has many other uses, such as for the measurement of temperatures over short time scales using cold-wire anemometry. Furthermore, with the growing field of micro-fluidics devices (Gad-el-Hak 2001), sensors such as the NSTAP could prove a complementary tool to existing instrumentation such as micro-PIV (particle-image velocimetry) by adding highly resolved, time-dependent measurements. Alternatively, such devices can be manufactured directly onto laboratory-on-a-chip devices for flow-rate measurement, or used to provide feedback in flow control applications.

This work was made possible by NSF MRI Grant CTS-0421147 and NSF Grant CTS-0625268, monitored by M. W. Plesniak and W. B. Schultz. The authors would also like to thank A. Ashok for his help setting up the grid turbulence measurements.

https://doi.org/10.1017/S0022112010003447 Published online by Cambridge University Press

REFERENCES

Adrian, R. J., Johnston, R. E., Jones, B. G., Meratit, P. & Tung, A. C.-T. 1984 Aerodynamic disturbances of hot-wire probes and directional sensitivity. *J. Phys.* E: *Sci. Instrum.* **14**, 62–71.

Avilov, V. V. & Decker, I. 1994 Heat transfer to laminar flow across plates and cylinders of various cross sections. *Pis'ma Zh. Eksp. Teor Fiz*. **59** (12), 851–855.

Bruun, H. H. 1995 *Hot-Wire Anemometry*. Oxford University Press.

Chen, J., Fan, Z., Zou, J., Engel, J. & Liu, C. 2003 Two-dimensional micromachined flow sensor array for fluid mechanics studies. *J. Aerosp. Engng* **16**, 85–97.

Chin, C. C., Hutchis, N., Ooi, A. S. H. & Marusic, I. 2009 Use of direct numerical simulation (DNS) data to investigate spatial resolution issues in measurements of wall-bounded turbulence. *Meas. Sci. Technol.* **20**, 115–401.

Citriniti, J. H. & George, W. K. 1997 The reduction of spatial aliasing by long hot-wire anemometer probes. *Exp. Fluids* **23**, 217–224.

Comte-Bellot, G. & Foss, J. F. 2007 Thermal anemometry. In *Springer Handbook of Experimental Fluid Mechanics* (ed. C. Tropea, A. L. Yarin & J. F. Foss), pp. 229–287. Springer.

Ewing, D., Hussein, H. J. & George, W. K. 1995 Spatial resolution of parallel hot-wire probes for derivative measurements. *Exp. Therm. Fluid Sci.* **11**, 155–173.

Fingerson, L. M. & Freymuth, P. 1983 Thermal anemometers. In *Fluid Mechanics Measurements* (ed. R. J. Goldstein), pp. 99–154. Hemisphere.

Gad-El-Hak, M. 2001 *The MEMS Handbook*. CRC Press.

Ho, C. M., Li, W., Garstenauer, M., Karan, K., Leu, T.-S. & Tai, Y.-C. 1993 Micromachined hot-point anemometer. Part II: Testing and calibration. *Bull. Am. Phys. Soc*. **38**, 2234.

Hutchins, N., Nickels, T. B., Marusic, I. & Chong, M. S. 2009 Hot-wire spatial resolution issues in wall-bounded turbulence. *J. Fluid Mech.* **635**, 103–136.

Jiang, F., Tai, Y.-C., Ho, C.-M., Karan, R. & Garstenauer, M. 1994 Theoretical and experimental studies of micromachined hot-wire anemometers. In *International Electron Devices Meeting, San Francisco, CA*, pp. 139–142. IEEE.

Klewicki, J. C. & Falco, R. E. 1990 On accurately measuring statistics associated with small-scale structure in turbulent boundary layers using hot-wire probes. *J. Fluid Mech.* **219**, 119–142.

Kunkel, G. J., Arnold, C. B. & Smits, A. J. 2006 Development of NSTAP: nanoscale thermal anemometry probe. In *36th AIAA Fluid Dynamics Conference and Exhibit, San Francisco, CA*, June 5–8, 2006, *AIAA Paper* 2006-3718.

Li, J. D. 2004 Dynamic response of constant temperature hot-wire system in turbulence velocity measurements. *Meas. Sci. Technol.* **15**, 1835–1847.

Li, J. D. 2006 Dynamic response of constant temperature hot-wire systems under various perturbations. *Meas. Sci. Technol.* **17**, 2665–2675.

Li, J. D., McKeon, B. J., Jiang, W., Morrison, J. F. & Smits, A. J. 2004 The response of hot wires in high-Reynolds-number turbulent pipe flow. *Meas. Sci. Technol.* **15**, 789–798.

Ligrani, P. M. & Bradshaw, P. 1987*a* Spatial resolution and measurement of turbulence in the viscous sublayer using subminiature hot-wire probes. *Exp. Fluids* **5**, 407–417.

Ligrani, P. M. & Bradshaw, P. 1987*b* Subminiature hot-wire sensors: development and use. *J. Phys.* E: *Sci. Instrum.* **20**, 323–332.

Löfdahl, L., Stemme, G. & Johannson, B. 1989 A sensor based on silicon technology for turbulence measurements. *J. Phys.* E: *Sci. Instrum.* **22**, 391–393.

Löfdahl, L., Stemme, G. & Johannson, B. 1992 Silicon based flow sensors for mean velocity and turbulence measurements. *Exp. Fluids* **12**, 391–393.

Morris, S. C. & Foss, J. F 2003 Transient thermal response of a hot-wire anemometer. *Meas. Sci. Technol.* **14**, 251–259.

Morrison, J. F., McKeon, B. J., Jiang, W. & Smits, A. J. 2004 Scaling of the streamwise velocity component in turbulent pipe flow. *J. Fluid Mech.* **508**, 99–131.

Perry, A. E., Smits, A. J. & Chong, M. S. 1979 The effect of certain low frequency phenomena on the calibration of hot wires. *J. Fluid Mech.* **90**, 415–431.

Tai, Y.-C., Jiang, F., Liu, C., Wu, R. & Ho, C. M. 1993 Micromachined hot-point anemometer. Part I: Design and fabrication. *Bull. Am. Phys. Soc*. **38**, 22–34.

Tavoularis, S. 2005 *Measurement in Fluid Mechanics*. Cambridge University Press.

https://doi.org/10.1017/S0022112010003447 Published online by Cambridge University Press

Willmarth, W. W. & Sharma, L. K. 1984 Study of turbulent structure with hot wires smaller than the viscous length. *J. Fluid Mech.* **142**, 121–149.

Wyngaard, J. C. 1968 Measurement of small-scale turbulence structure with hot-wires. *J. Phys.* E: *Sci. Instrum.* **2**(2), 1105–1108.

Yakhot, V., Bailey, S. C. C. & Smits, A. J. 2010 Scaling of global properties of turbulence and skin friction in pipe and channel flows. *J. Fluid. Mech.* **652**, 65–73.

Zagarola, M. V. & Smits, A. J. 1998 Mean flow scaling of turbulent pipe flow. *J. Fluid. Mech.* **373**, 33–79.

https://doi.org/10.1017/S0022112010003447 Published online by Cambridge University Press